Plasmonic Mach-Zehnder Interferometers Based on Air-Gap Couplers

Rami A. Wahsheh

***Abstract*—Mach-Zehnder interferometers (MZIs) are vital in optical biosensor applications and high-density integrated photonic circuits. In this research work, we theoretically investigate the design steps of MZIs, consisting of 3-dB plasmonic splitters sandwiched between two dielectric waveguides with an air-gap coupler at the interface from each side. The proposed MZI designs feature a compact size, ensuring high transmission coupling efficiency without introducing additional radiation or reflection losses, as observed in tapered, T- and Y-shaped splitters. The analytical results and simulations prove that the proposed MZI designs offer a broad spectrum range with a high fabrication tolerance and the ability to use them in all-optical plasmonic circuits.**

***Index Terms*—Dielectric waveguide, integrated optics devices, Mach-Zehnder interferometer, nanoplasmonic waveguides, splitter, surface plasmon polariton.**

I. Introduction

THE unique properties of the metal-dielectric-metal (MDM) plasmonic waveguides, overcoming the diffraction limit of the conventional dielectric waveguides (CDWs) and strong field confinement in the dielectric region, have made MDM plasmonic waveguides play a vital role in the miniaturization of low cost and high-density photonic integrated circuits [1], [2], [3], [4]. The potential of using MDM plasmonic waveguides in many optical devices has been explored. MDM plasmonic waveguides have been used in several applications, including power splitters [5], [6], [7], [8], [9], [10], [11], Mach-Zehnder interferometers [12], [13], [14], [15], filters [16], [17], [18], [19], switches [20], [21], [22], [23], sensors [24], [25], [26], [27], wavelength division multiplexers [28], [29], [30], solar cells [31], [32], [33], [34], and photovoltaic devices [35], [36], [37], [38]. To design high-performance nanoscale plasmonic devices and increase the information processing speed, a hybrid integration of plasmonic and CDW is required. The low-loss CDWs transmit the optical signal into and out of the plasmonic waveguides. Therefore, several different coupling structures have been investigated to funnel light from the CDWs into the MDM plasmonic waveguides [39], [40], [41], [42], [43], [44]. In [39], the authors proposed a semi-elliptical nanoplasmonic coupler at the interface, achieving a coupling efficiency of ∼85%. In [40], the authors used multisection tapers inside the CDW and the MDM waveguides and reported a coupling efficiency above ∼93%. In [41], the authors used vertical and lateral tapered silicon waveguides, reporting a coupling efficiency above ∼87%. The proposed couplers either have large dimensions or are challenging to fabricate. In [42], we used a very short air-slot coupler at the interface between the CDW and the MDM waveguides, achieving a theoretical coupling efficiency of ∼86% and experimental transmission coupling efficiency (TCE) of less than ∼40% [43]. In [44], we reported different designs of very compact air-gap couplers (AGCs) at the interface between a 300 nm wide CDW and two 40 nm wide MDM plasmonic waveguides, achieving a coupling efficiency above ∼93%. Based on those proposed couplers, we proposed plasmonic splitter designs in [5] without considering the effect of sandwiching the MDM plasmonic waveguide between two dielectric waveguides. For practical applications of our proposed plasmonic splitters in [5], the MDM plasmonic waveguides was sandwiched between two CDWs to couple light into and out of the MDM plasmonic waveguides. In this research, we continue our previous work in [45] and connect the proposed designs in [5] back-to-back. In this configuration, the two MDM plasmonic waveguides form the two arms of the Mach-Zehnder interferometer (MZI).

To the best of our knowledge, none of the previously proposed MZIs in the literature have addressed the specific challenge of coupling from a dielectric waveguide into a plasmonic waveguide and back into the dielectric waveguide. This coupling process, which we have considered in our present and previous research documented in [12], sets our work apart. In both studies, we connected two 3-dB splitters consecutively to create an MZI. This design utilized a silver-air-silver geometry and AGCs at each interface between the two types of waveguides. In our earlier work described in [12], the AGC was situated within the metal region, whereas in our current research, it is positioned within the dielectric and metal regions. Furthermore, we incorporated a tapered dielectric waveguide in the present configuration before connecting it to the AGC. This alteration resulted in significantly enhanced coupling efficiency compared to the previous design, notably reduced oscillations in the measured TCE. These oscillations were attributed to the Fabry-Perot (FP) cavity-like response caused by the reflection of the plasmon mode from each dielectric waveguide. To the best of our knowledge, our proposed MZI surpasses the performance of all previously reported works in the literature on multiple fronts, including size, TCE, and fabrication tolerance.

Manuscript received 18 September 2023; revised 25 October 2023; accepted 30 October 2023. Date of publication 3 November 2023; date of current version 16 November 2023.

The author is with the Communications Engineering Department, Princess Sumaya University for Technology, Amman 11941, Jordan (e-mail: r.wahsheh@psut.edu.jo).

Digital Object Identifier 10.1109/JPHOT.2023.3329940

The parameters of the MZI's geometry and the spectrum response of the proposed MZI designs are studied using the two-dimensional finite difference time domain (2D-FDTD) method. We opted not to use a three-dimensional (3D) simulation due to its significantly higher run time and memory requirements than a 2D simulation. Instead, we conducted 2D-FDTD simulations using a mesh size of 1 nm to accurately capture interface changes between the CDW and the MDM plasmonic waveguides. While our simulations considered metal losses, we excluded losses related to the CDWs because they have very short lengths in our setup. For evaluation, we measured the TCE within the output CDW and the back reflection power (BRP) within the input CDW, in which both measurements are normalized relative to the incident power. All simulations are performed at the optical communications wavelength 1550 nm, while the spectrum response is done for 400 nm to 2400 nm wavelengths.

In our study, we begin by examining the impact of sandwiching the MDM plasmonic waveguides between two CDWs by increasing the length of the embedded two MDM plasmonic waveguides and evaluating the TCE into the output CDW. Then, we keep the lengths of the two MDM plasmonic waveguides constant and compare the spectrum responses of different MZI designs to demonstrate that sandwiching the MDM plasmonic waveguide between two CDWs results in a narrowed spectrum response due to the FP cavity-like response [46]. Furthermore, we investigate the fabrication tolerance associated with the proposed MZI that exhibits the highest TCE. This involves altering various parameters of the design dimensions and analyzing their effects on the spectrum response. Our numerical demonstrations underscore the practical applications of these proposed designs, particularly in integrating ultracompact nanoplasmonic circuits.

The subsequent sections of this paper are structured as follows. Section II presents the schematics of the proposed MZI designs with their simulation results and a discussion of the relationship between TCE and the lengths of the two MDM plasmonic waveguides. In addition, we conduct a comparative analysis of the spectrum results obtained from the proposed designs and show the possibility of using one of the designs in biosensing applications. Section III focuses on investigating the fabrication tolerance of the proposed MZI design that resulted in the highest TCE, emphasizing its ability to function effectively with less alignment precision. Lastly, Section IV offers concluding remarks based on the findings and implications discussed throughout the paper.

II. Schematics, Simulation Results, and Spectrum Responses of the Proposed MZI Designs

Several T- and Y-shaped splitters have been proposed [47], [48], [49], [50], [51], [52]. These shapes typically have large dimensions, leading to radiation or reflection losses in addition to propagation losses in the waveguides used for light splitting. To advance the development of the next generation of integrated photonic circuits for signal interconnection, it is essential to design compact MZIs with a broad spectrum range, avoiding additional radiation or reflection losses while allowing control over the power splitting ratio. In our research work, we have successfully addressed these challenges by introducing MZI designs that achieve all these requirements. Our proposed compact-size splitters offer a broad spectrum range without inducing additional radiation or reflection losses, providing precise control over the power splitting ratio.

In this research work, we propose six MZI designs based on the location of the AGC and on whether the CDW is tapered before it is connected to the AGC. The CDW is tapered to improve the TCE. In each MZI's design, we use AGC #1, AGC #2, or AGC #3. AGC #1 is located at the interface inside the metal region, AGC #2 is located at the interface inside the dielectric region, and AGC #3 extends equally inside both types of materials. The dimensions of AGCs #1, #2, and #3 are (width $\times$ length) 260 nm $\times$ 15 nm, 210 nm $\times$ 20 nm, and 240 nm $\times$ 20 nm, respectively [44]. The input and output CDWs, including the AGCs, are identical in each design. The parameters of the proposed structures are shown in Fig. 1. As shown in Fig. 1(a)–(f), the proposed six designs are as follows: MZI #1 uses AGC #1 without tapering the CDWs, MZI #2 is the same as MZI #1 but with tapering the CDWs, MZI #3 uses AGC #2 without tapering the CDWs, MZI #4 is the same as MZI #3 but with tapering the CDWs, MZI #5 uses AGC #3 without tapering the CDWs, and MZI #6 is the same as MZI #5 but with tapering the CDWs. The dimensions of the tapered CDWs for MZIs #2, #4, and #6 are (width $\times$ length) 380 nm $\times$ 330 nm, 380 nm $\times$ 340 nm, and 380 nm $\times$ 330 nm, respectively [44]. The separation distances between each design's two MDM plasmonic branches are 210 nm, 240 nm, 200 nm, 200 nm, 210 nm, and 240 nm, respectively [5]. In each configuration, the incident light in the input CDW undergoes an equal split into both branches of the MDM plasmonic waveguides. Subsequently, the light is recombined at the output CDW. The two branches of the MDM plasmonic waveguides collectively constitute the two propagation arms of the MZI.

Fig. 2 demonstrates the impact of varying the length of the two MDM plasmonic branches (L_{MZI}) on the TCE for all the proposed six MZI designs. MZIs #2 and #6 exhibit higher TCE values with minimal oscillations in the measured data. Designs #2 and #6 display nearly identical results, aligning closely on the graph. In contrast, designs #1, #3, #4, and #5 showcase more pronounced oscillations in their TCE results. The observed oscillations are attributed to the FP cavity-like structure arising from the MDM plasmonic branches sandwiched between the two CDWs. Concurrently, the reduction in the amplitude of the TCE as L_{MZI} increases from 100 nm to 2500 nm is linked to the propagation losses resulting from the metallic interactions.

Although MZIs #2 and #6 yield nearly identical TCE values, we opt for the latter as our best proposed MZI design due to its lower fabrication precision requirements, as highlighted in [6]. Additionally, positioning the AGC at the interface between two materials is simpler than precise placement within a specific material. With MZI #6, as long as there is an overlap between the AGC and both materials, efficient light coupling occurs into and out of the two MDM plasmonic branches.

All of our proposed MZI designs operate at a broad frequency range. To demonstrate this, we performed simulations where we varied the wavelength of the light source from 400 nm

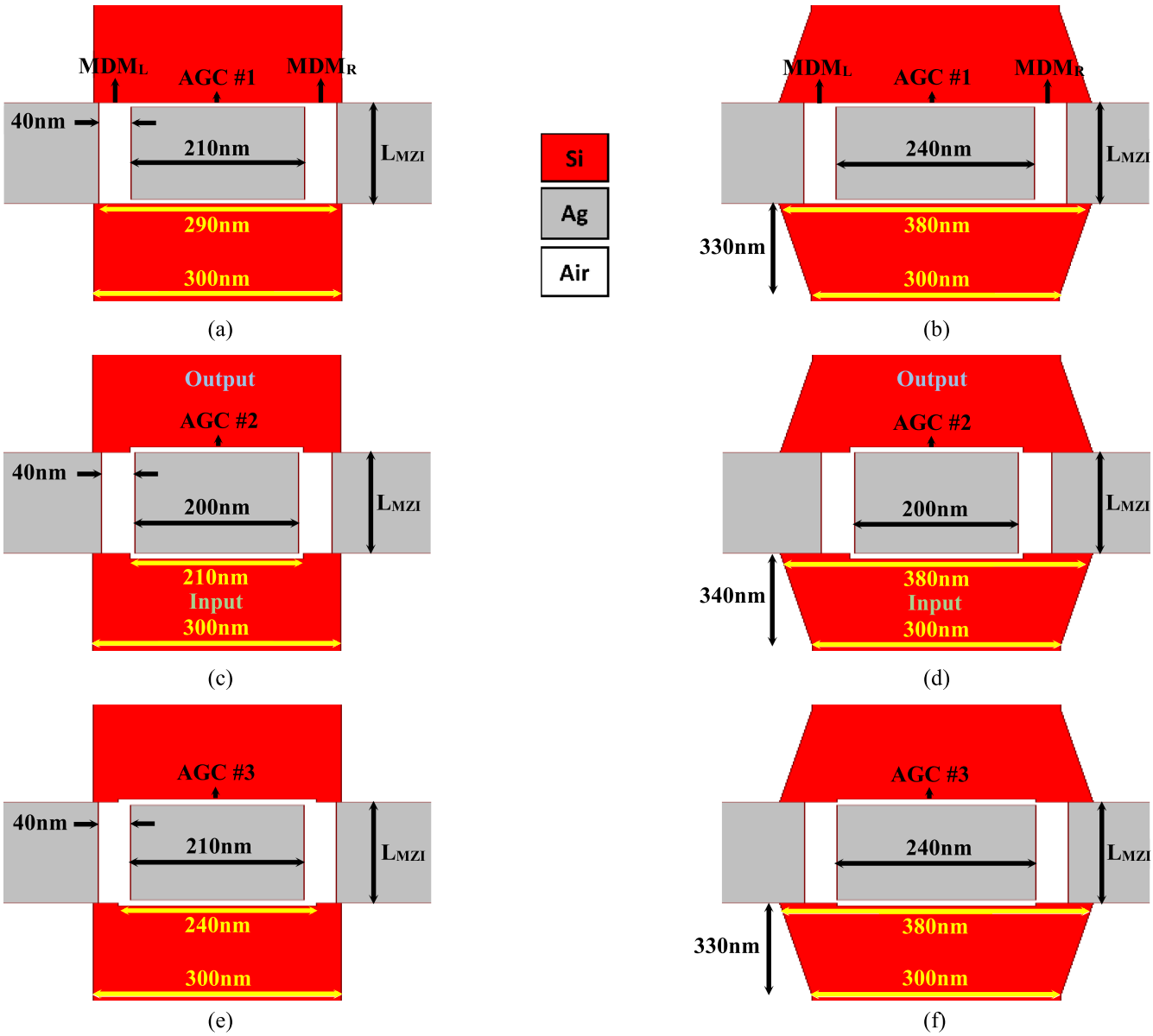

Fig. 1. Schematics of the proposed MZI designs illustrate how light is coupled into and out of the sandwiched MDM plasmonic waveguides. The designs are as follows: (a) MZI #1 utilizes AGC #1 without tapering the CDWs. (b) MZI #2 is similar to MZI #1 but incorporates tapering the CDWs. (c) MZI #3 employs AGC #2 without tapering the CDWs. (d) MZI #4 is similar to MZI #3 but includes tapering the CDWs. (e) MZI #5 utilizes AGC #3 without tapering the CDWs. (f) MZI #6 is similar to MZI #5 but incorporates tapering the CDWs.

to 2400 nm and evaluated the corresponding TCE at each wavelength. Fig. 3 displays the spectra of all the proposed six MZI designs. The chosen values for L_{MZI} for each of the six MZI designs shown in Fig. 1(a)–(f) are as follows: 625 nm, 575 nm, 650 nm, 550 nm, 625 nm, and 550 nm, respectively. These specific lengths were selected to correspond to where the second peak occurs, as indicated in Fig. 2. In addition, we included the spectra of the proposed six splitters without the MDM plasmonic waveguides being sandwiched between the two CDWs [5]. In this case, the measured coupling efficiency in the unsandwiched MDM waveguides is obtained within one of the MDM plasmonic branches. Each MDM branch has 50% of the total coupled light. That is why the measured coupling efficiency for the unsandwiched MDM waveguides is almost half that of the sandwiched ones. This setup enabled us to compare the spectrum response of the unsandwiched MDM plasmonic waveguides with that of our proposed MZI designs. As shown in Fig. 3, incorporating the MDM plasmonic waveguides between two CDWs reduces the spectrum width and alters its shape compared to the designs without the sandwiching arrangement. In addition, all MZI designs showed almost a flat spectrum response from 1260 nm to 1625 nm, which covers all the five wavelength bands referred to as the O-, E-, S-, C-, and L-bands.

Fig. 4 provides a visual representation of the sensitivity of MZI #6 to variations in the refractive index (n) within both the MDM plasmonic branches and the AGCs. With n set at 1.00 (representing air), MZI #6 demonstrates a broad-spectrum response. However, as n incrementally rises from 1.00 to 2.00,

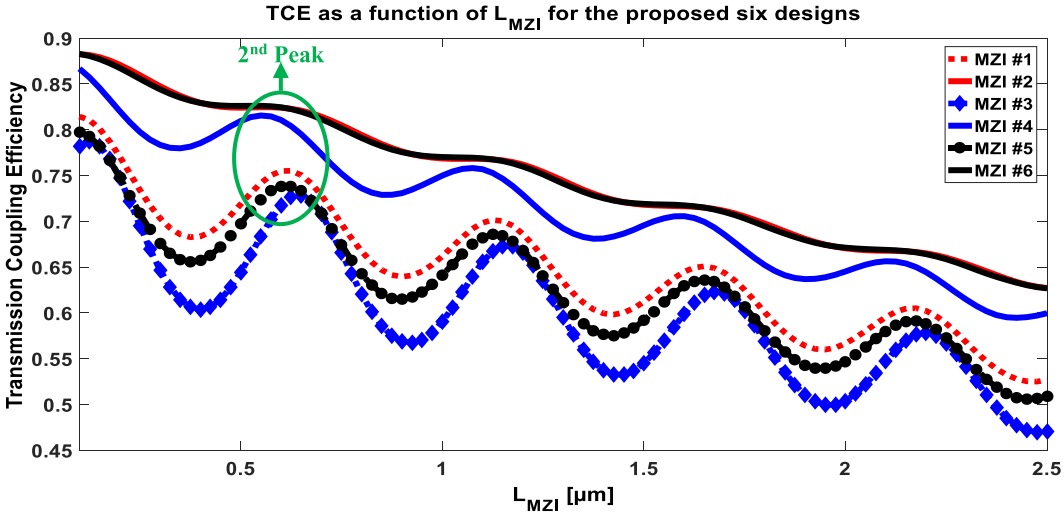

Fig. 2. TCE is plotted as a function of the length of the MDM plasmonic waveguide, L_{MZI}, for all the proposed six MZI designs depicted in Fig. 1.

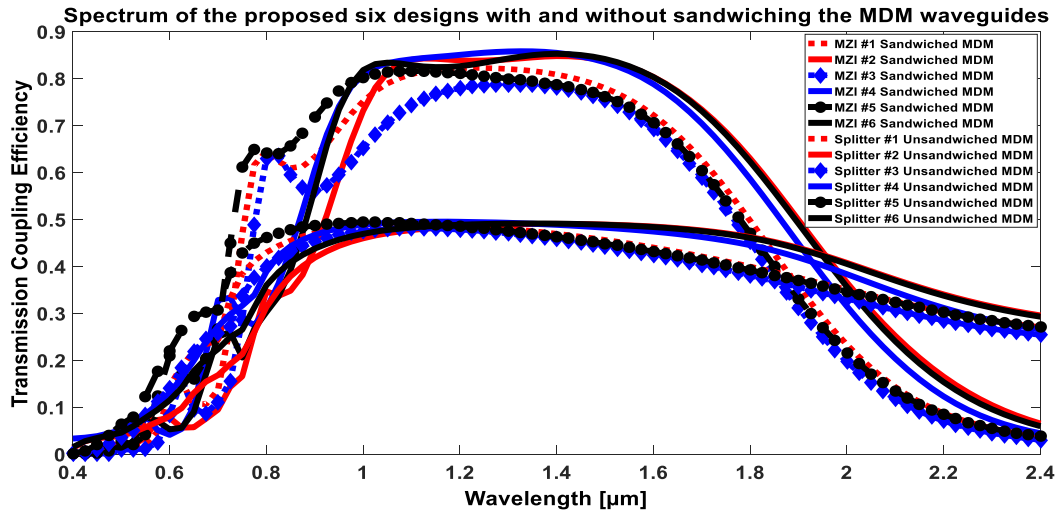

Fig. 3. Spectra of the proposed six MZI designs and those of the same six designs without sandwiching the MDM plasmonic waveguides.

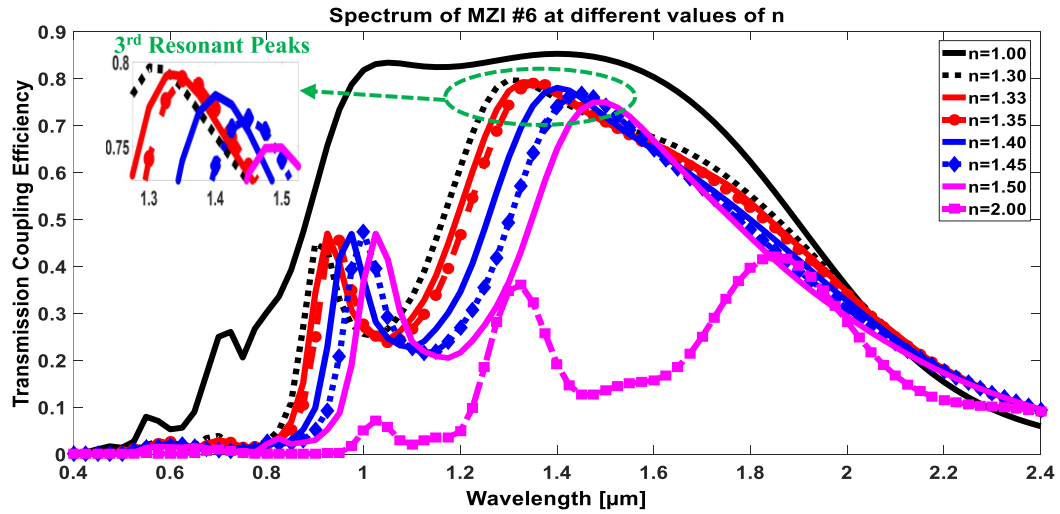

Fig. 4. Spectrum of MZI #6 at different values of the refractive indices, n, of the MDM plasmonic waveguides and that of the AGCs.

the TCE diminishes, giving rise to three distinct resonance peaks characterized by varying amplitudes and widths, accompanied by a smaller peak with an indistinct width. This stands in contrast to the initial single, broad spectrum range housing a dominant peak. The reduction in TCE is ascribed to less efficient coupling into and out of the two MZI branches. The shift in the resonant wavelengths is a consequence of the FP cavity-like structure responding to changes in n. This particular attribute underscores the practicality of MZI #6 in detecting variations in the refractive index, particularly in the context of numerous biological applications. For example, it can distinguish cancerous skin cells ($n = 1.38$) from healthy skin cells ($n = 1.36$), as well as differentiate various components of blood, such as water ($n = 1.33$), red blood cells ($n = 1.34$), plasma ($n = 1.35$), white blood cells ($n = 1.36$), and hemoglobin ($n = 1.38$) [53]. Fig. 4 provides a clear representation of how the resonant wavelengths adapt in response to changes in the refractive index of biological components. The selection of the third resonant peak for detecting refractive index changes is due to its highest TCE and its capability to discern minor variations in n. This will be the subject of further exploration in an upcoming research publication.

III. Fabrication Precision Requirements

The proposed fabrication process for creating MZI #6 on a silicon-on-insulator wafer follows a series of steps, as outlined in reference [43]. Electron-beam lithography is employed to delineate alignment marks in specific positions precisely. Following this, a layer of gold is applied to make these marks visible, enabling their examination under a scanning electron microscope (SEM). These alignment marks are pivotal in accurately positioning the dielectric waveguides in their designated locations. In the final phase, these same alignment marks are repurposed to mark the regions where metal deposition is needed to define the plasmonic waveguides. The focused ion beam (FIB) technique is employed to define the MDM plasmonic waveguides, including the AGCs, meticulously. Furthermore, the FIB is utilized to deposit a layer of platinum on top of the metal layer. This step is fundamental to achieving a slot waveguide with a rectangular shape, ensuring that the width at the top matches that at the bottom. Without this adjustment, the MDM waveguide would take on a triangular profile, with its upper section being broader than its base.

A 3-dB splitting ratio can be achieved by having two identical MDM plasmonic branches (MDM_L and MDM_R) with the same width and location from the center of the dielectric waveguide. Breaking this symmetry between the two MDM plasmonic branches by different fabrication errors causes unequal splitting ratios into MDM_L and MDM_R. In this research work, we will show the impact of the mismatches in the fabricated structure dimensions compared to that of the optimized values on the overall performance of the best proposed MZI design #6. The effects of changing different parameters of the MZI's geometry due to fabrication errors, such as the separation distance (D) between the two MDM plasmonic waveguides, the width of the two MDM plasmonic branches (W_L or W_R), and the location of the two MDM plasmonic waveguides (d) with respect to the center of the CDW, are shown in Figs. 5, 6, and 7, respectively. These parameters are susceptible to lithography and etching biases, significantly influencing the device performance control. We modified one individual parameter while maintaining the remaining ones at their optimal values, observing their impact on the TCE, BRP, and spectrum response. The optimal values of D, W_L, W_R, and d are 240 nm, 40 nm, 40 nm, and 0 nm, respectively. These parameters mainly dictate the size of the supported mode, consequently shaping the spectrum response of the proposed design. Although mode size holds importance, other factors come into play. Notably, the formation of an FP cavity-like structure, a consequence of sandwiching the MDM plasmonic waveguide between two CDWs (specifically L_{MZI}), also contributes to determining the wavelengths supported in resonance.

Different methods could be applied to investigate the effect of varying the separation distance (D) between the two MDM branches (MDM_L and MDM_R) on the TCE. One method is by keeping the location of one of the MDM branches at its optimum location and displacing the other one from its optimum location while measuring the TCE and the BRP. For example, if the center of MDM_R is kept fixed at the exact optimum location (which is 140 nm away from the center of CDW), while MDM_L is moved away from MDM_R in steps of 10 nm (see Fig. 5(a)). During this process, we measure the TCE and BRP at every step at 1550 nm to assess their variations, as shown in Fig. 5(b). To determine the variation of the TCE over different wavelengths, Fig. 5(c) shows the TCE spectrum response for different values of D. When $D = 0$ nm, there is no space between MDM_L and MDM_R as if we have one wide MDM branch with a width of 80 nm. As D increases from 0 nm to 230 nm, more light couples into MDM_L than that into MDM_R. This happens because the surface plasmons polariton (SPP) excitation starts at the metal-air interface that is closer to MDM_L, leading to more light that couples into the closer waveguide MDM_L than that into the further waveguide MDM_R; see Fig. 5(d) for the case when $D = 70$ nm (measured at 1550 nm). At $D = 240$ nm (measured at 1550 nm), maximum TCE with almost zero BRP occurs because this is where SPP starts at an equal distance from both branches and consequently, 3-dB splitting is achieved (see Fig. 5(e)). When D is between 240 nm and 300 nm, the TCE decreases and BRP increases because MDM_L is no longer connected to the AGC, but still, a tiny light manages to funnel into MDM_L. Fig. 5(f) shows that when $D = 260$ nm (measured at 1550 nm), the excited SPP starts away from MDM_R at the metal-dielectric interface closer to MDM_L and inside the AGC. The excited SPP requires a longer distance to propagate to MDM_R and, consequently, more propagation losses and less light funnels into MDM_R. This proves that the location of the two MDM plasmonic waveguides introduces transverse metal boundaries that controls the starting area of the SPP excitation. When D is more significant than 300 nm, no light funnels into MDM_L, and the TCE and the BRP stay constant.

Another parameter in the MZI's geometry that, if changed from its optimum value, causes an unequal splitting ratio between the two MDM plasmonic branches, when the two MDM

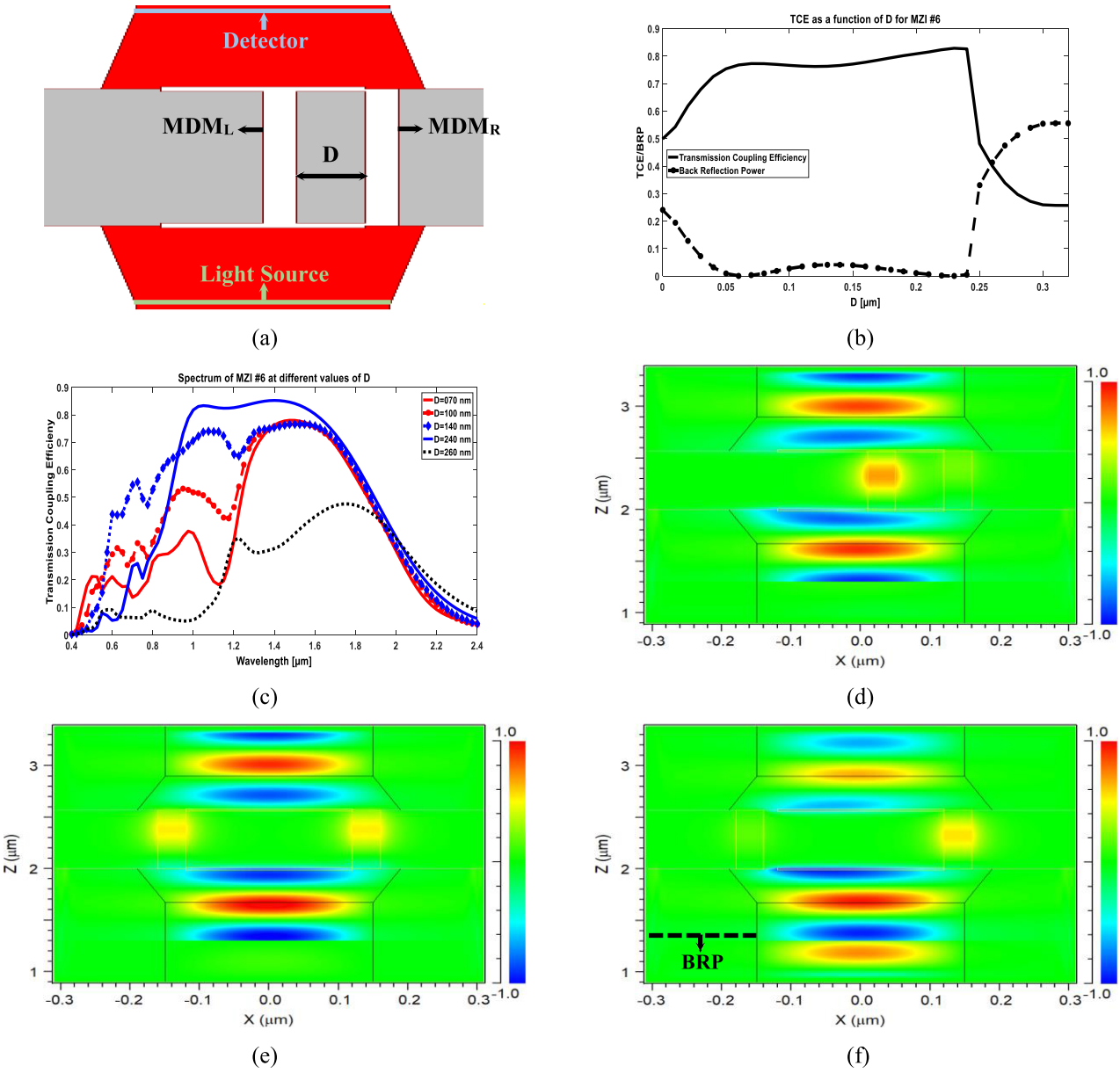

Fig. 5. (a) Schematic diagram illustrates how the TCE and the BRP are affected by the separation distance (D) between the two MDM waveguides for the proposed MZI #6. (b) TCE and BRP are plotted as a function of D (measured at 1550 nm). (c) The TCE spectrum response for different values of D. (d) The field distribution at $D = 70$ nm demonstrates that the SPP excitation starts away from both branches. (e) The field distribution at $D = 240$ nm illustrates that the SPP excitation begins between the two MDM branches. (f) The field distribution at $D = 260$ nm shows that the SPP excitation starts inside the AGC at the side closer to MDM_L.

plasmonic waveguides MDM_L and MDM_R have unequal widths W_L and W_R, respectively, see Fig. 6(a). To investigate that, the width of one of the MDM plasmonic branches is changed while the other one is unchanged while measuring the TCE and the BRP at 1550 nm, see Fig. 6(b). For example, if W_L is kept at 40 nm and W_R is changed from 40 nm to 280 nm, then the variation of the TCE over different wavelengths can be assessed; Fig. 6(c) shows the TCE spectrum response for different values of W_R. The direction of the increase in W_R is towards the MDM_L while keeping the other side of MDM_R at 280 nm from MDM_L. When $W_R = 280$ nm, the two MDM plasmonic branches become one wide waveguide with a combined width of 320 nm. As shown in Fig. 6(b), by increasing the width of W_R by 10 nm, the TCE slightly increases from 82.6% to 83.3% because more light couples into MDM_R than into MDM_L. As W_R increases, less light funnels into MDM_L than into MDM_R, even though SPP excitation always starts away from MDM_R and closer to MDM_L; see Fig. 6(d) for the case when $W_R = 100$ nm (measured at 1550 nm). This proves that more light couples into the wider waveguide than into the narrower one. Also, TCE decreases as W_R increases due to the increase in the BRP caused by the reduction in the interacted width of the metal-air interface inside the AGC; see Fig. 6(e) for the case when $W_R = 220$ nm (measured at 1550 nm). When $W_R = 280$ nm (see Fig. 6(f),

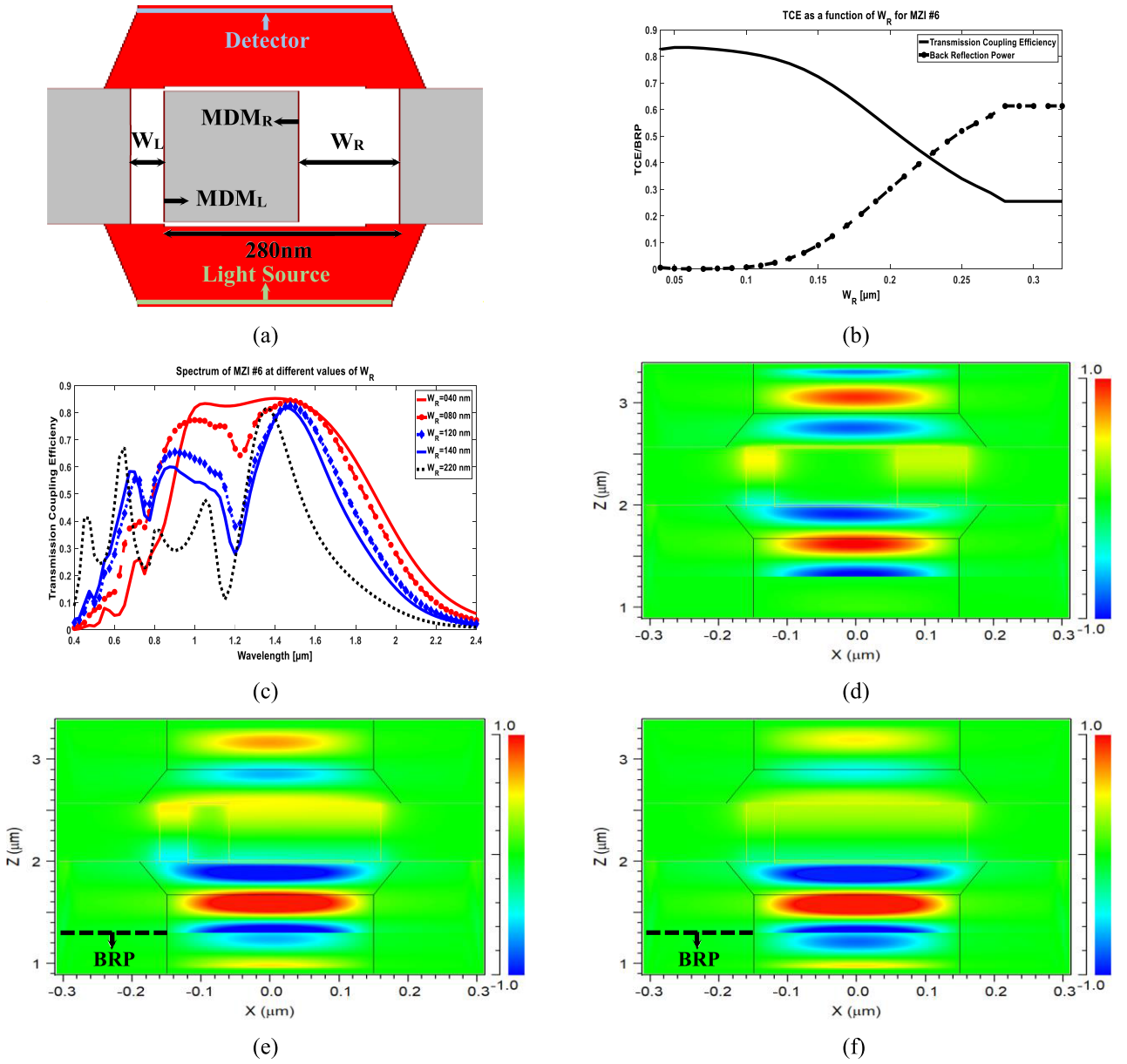

Fig. 6. (a) Schematic diagram illustrates how the TCE can be controlled by varying the width of W_R while keeping that of the other MDM plasmonic waveguide, W_L, unchanged for the proposed MZI #6. (b) The plot showcases the TCE and the BRP as a function of W_R (measured at 1550 nm). (c) The TCE spectrum response for different values of W_R. (d) The field distribution corresponds to the configuration outlined in (a) when measured at 1550 nm, with W_R set at 100 nm. (e) Similarly, the field distribution pertains to the format described in (a), but with W_R set at 220 nm. (f) Also, the field distribution relates to the configuration illustrated in (a), but with W_R set at 280 nm.

which is measured at 1550 nm), the two plasmonic waveguides become one wide waveguide, which is why the same TCE and BRP occurred from $W_R = 280$ nm to 320 nm.

Additionally, the proposed coupler exhibits considerable alignment tolerance between the CDWs and the MDM plasmonic waveguides (including the AGC), which is crucial for practical applications. The AGC is considered with the MDM plasmonic waveguides as one group because if, for example, the FIB is used, then those two together are defined simultaneously. Misalignment between the center of the AGCs (with the two MDM plasmonic waveguides) and the center of the CDWs, represented by the displacement (d) in Fig. 7(a), affects the splitting ratio between the two MDM plasmonic branches. For example, if the locations of the two MDM plasmonic waveguides, including the AGCs, are kept fixed at the exact optimum location, while the two CDWs were moved away to the right-hand side in steps of 10 nm (see Fig. 7(a)). During this process, we measure the TCE and BRP at every step at 1550 nm to assess their variations, as shown in Fig. 7(b). To determine the variation of the TCE over different wavelengths, Fig. 7(c) shows the TCE spectrum response for different values of d. For values of d less than 130 nm, the TCE results from the funneled light from both MDM plasmonic branches, see Fig. 7(d) when $d = 70$ nm (measured at 1550 nm). As d increases, the BRP increases because the SPP

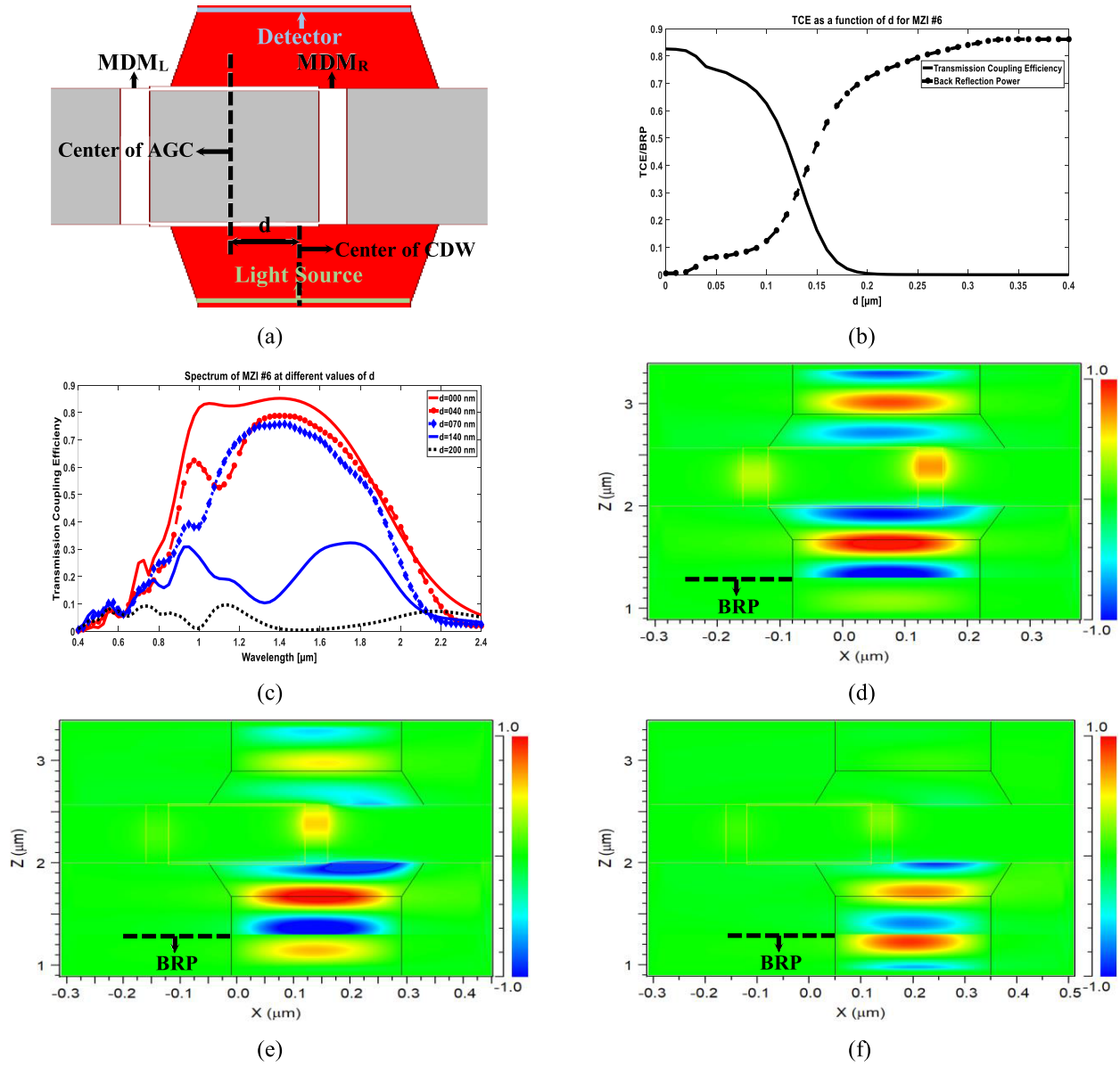

Fig. 7. (a) Schematic diagram illustrates how the TCE and the BRP are affected as a function of the position misalignment, d, between the center of the AGCs (with the two MDM plasmonic waveguides) and the center of the CDWs for the proposed MZI #6. (b) TCE and BRP as a function of d (measured at 1550 nm). (c) The TCE spectrum response for different values of d. (d) Field distribution for the schematic shown in (a) when $d = 70$ nm (measured at 1550 nm). (e) Field distribution for the schematic shown in (a) when $d = 140$ nm (measured at 1550 nm). (f) Field distribution for the schematic shown in (a) when $d = 200$ nm (measured at 1550 nm).

excitation starts at the dielectric-metal boundary and not inside the AGC, as shown in Fig. 7(e) when $d = 130$ nm (measured at 1550 nm), more light couples into the closer waveguide MDM_R than into the further waveguide MDM_L. At $d = 130$ nm, the TCE is from the funneled light into only the MDM_R. The increase in the BRP continues as d increases, and the TCE reaches almost zero at $d = 200$ nm (measured at 1550 nm); see Fig. 7(f). Even though the TCE is nearly zero at $d = 200$ nm, the BRP continues to increase as d increases because more light is reflected into the input CDW, and less light is coupled into the AGC that is not bounded by the CDW. This proves that overlapping the two MDM branches, including the AGC and the CDW, is necessary to achieve high TCE in both MDM branches.

IV. Conclusion

In this study, a proposal and optimization of highly efficient MZIs were presented, comprising two 40 nm wide silver-air-silver plasmonic waveguides sandwiched between two 300 nm wide Si waveguides with two very compact air-gap couplers (AGCs) at the interface between both types of waveguides. Two configurations of these MZIs demonstrated excellent transmission coupling efficiency (TCE). Furthermore, when embedding the MDM plasmonic waveguide between two CDWs, we observed a Fabry-Perot cavity-like structure, resulting in a narrower spectrum response than that without sandwiching the MDM waveguides. The practicality of one of the MZI designs

that resulted in the highest TCE for sensing changes in the refractive index inside the MDM plasmonic waveguides and the AGCs makes it a valuable asset in biosensor applications. Additionally, our study analyzed the spectrum response for different key design parameters, highlighting the impact of mismatches in fabricated structure dimensions compared to optimized values on overall performance. The proposed structure holds potential for utilization in diverse high-density photonic integration circuits.

References

[1] E. N. Economou, "Surface plasmons in thin films," *Phys. Rev.*, vol. 182, no. 2, pp. 539–554, Jun. 1969, doi: 10.1103/PhysRev.182.539.

[2] E. Ozbay, "Plasmonics: Merging photonics and electronics at nanoscale dimensions," *Science*, vol. 311, no. 5758, pp. 189–193, Jan. 2006, doi: 10.1126/science.1114849.

[3] D. K. Gramotnev and S. I. Bozhevolnyi, "Plasmonics beyond the diffraction limit," *Nature Photon.*, vol. 4, no. 2, pp. 83–91, Feb. 2010, doi: 10.1038/nphoton.2009.282.

[4] R. F. Oulton, V. J. Sorger, D. A. Genov, D. F. P. Pile, and X. Zhang, "A hybrid plasmonic waveguide for subwavelength confinement and long-range propagation," *Nature Photon.*, vol. 2, no. 8, pp. 496–500, Aug. 2008, doi: 10.1038/nphoton.2008.131.

[5] R. A. Wahsheh, "Ultra-compact broadband 3-dB metal-dielectric-metal plasmonic power splitter," *J. Modern Opt.*, vol. 68, no. 3, pp. 153–160, Feb. 2021, doi: 10.1080/09500340.2021.1884299.

[6] R. A. Wahsheh, Z. Lu, and M. A. G. Abushagur, "Integrated nanoplasmonic splitter," *High Capacity Opt. Netw. Emerg./Enabling Technol.*, Magosa, Cyprus, 2013, pp. 155–156, doi: 10.1109/HONET.2013.6729776.

[7] R. A. Wahsheh, Z. Lu, and M. A. G. Abushagur, "Nanoplasmonic couplers and splitters," *Opt. Exp.*, vol. 17, no. 21, pp. 19033–19040, Oct. 2009, doi: 10.1364/OE.17.019033.

[8] C.-H. Chen and K.-S. Liao, "1xN plasmonic power splitters based on metal-insulator-metal waveguides," *Opt. Exp.*, vol. 21, no. 4, pp. 4036–4043, Feb. 2013, doi: 10.1364/OE.21.004036.

[9] K. Wen, Y. Hu, L. Chen, J. Zhou, L. Lei, and Z. Meng, "Plasmonic bidirectional/unidirectional wavelength splitter based on metal-dielectric-metal waveguides," *Plasmonics*, vol. 11, pp. 71–77, Jul. 2015, doi: 10.1007/s11468-015-0021-4.

[10] X. Shi, W. Yang, H. Xing, and X. Chen, "Design of power splitters based on hybrid plasmonic waveguides," *Appl. Sci.*, vol. 11, no. 18, Sep. 2021, Art. no. 8644, doi: 10.3390/app11188644.

[11] H.-S. Chu, P. Bai, E.-P. Li, and W. R. J. Hoefer, "Hybrid dielectric-loaded plasmonic waveguide-based power splitter and ring resonator: Compact size and high optical performance for nanophotonic circuits," *Plasmonics*, vol. 6, pp. 591–597, May 2011, doi: 10.1007/s11468-011-9239-y.

[12] R. A. Wahsheh, Z. Lu, and M. A. G. Abushagur, "Nanoplasmonic directional couplers and Mach–Zehnder interferometers," *Opt. Commun.*, vol. 282, no. 23, pp. 4622–4626, Dec. 2009, doi: 10.1016/j.optcom.2009.08.045.

[13] Y. Gao, Q. Gan, Z. Xin, X. Cheng, and F. J. Bartoli, "Plasmonic Mach–Zehnder interferometer for ultrasensitive on-chip biosensing," *Amer. Chem. Soc. Nano*, vol. 5, no. 12, pp. 9836–9844, Nov. 2011, doi: 10.1021/nn2034204.

[14] S. Kamada, T. Okamoto, S. E. El-Zohary, and M. Haraguchi, "Design optimization and fabrication of Mach-Zehnder interferometer based on MIM plasmonic waveguides," *Opt. Exp.*, vol. 24, no. 15, pp. 16224–16231, Jul. 2016, doi: 10.1364/OE.24.016224.

[15] Z. Han, L. Liu, and E. Forsberg, "Ultra-compact directional couplers and Mach-Zehnder interferometers employing surface plasmon polaritons," *Opt. Commun.*, vol. 259, no. 2, pp. 690–695, Mar. 2006, doi: 10.1016/j.optcom.2005.09.034.

[16] B. Yun, G. Hu, and Y. Cui, "Resonant mode analysis of the nanoscale surface plasmon polariton waveguide filter with rectangle cavity," *Plasmonics*, vol. 8, pp. 267–275, Jun. 2013, doi: 10.1007/s11468-012-9384-y.

[17] Z. Zhang, F. Shi, and Y. Chen, "Tunable multichannel plasmonic filter based on coupling-induced mode splitting," *Plasmonics*, vol. 10, pp. 139–144, Feb. 2015, doi: 10.1007/s11468-014-9787-z.

[18] Y. Qi et al., "Theoretical study of a multichannel plasmonic waveguide notch filter with double-sided nanodisk and two slot cavities," *Results Phys.*, vol. 14, Sep. 2019, Art. no. 102506, doi: 10.1016/j.rinp.2019.102506.

[19] Y. -F. C. Chau, C. -T. C. Chao, and H. -P. Chiang, "Ultra-broad bandgap metal-insulator-metal waveguide filter with symmetrical stubs and defects," *Results Phys.*, vol. 17, Jun. 2020, Art. no. 103116, doi: 10.1016/j.rinp.2020.103116.

[20] Z. Yu, G. Veronis, S. Fan, and M. L. Brongersma, "Gain-induced switching in metal-dielectric-metal plasmonic waveguides," *Appl. Phys. Lett.*, vol. 92, no. 4, Jan. 2008, Art. no. 041117, doi: 10.1063/1.2839324.

[21] A. N. Taheri and H. Kaatuzian, "Design and simulation of a nanoscale electro-plasmonic 1×2 switch based on asymmetric metal-insulator-metal sub filters," *Appl. Opt.*, vol. 53, no. 28, pp. 6546–6553, Oct. 2014, doi: 10.1364/ao.53.006546.

[22] R. Negahdari, E. Rafiee, and F. Emami, "Realization of all-optical plasmonic MIM split square ring resonator switch," *Opt. Quantum Electron.*, vol. 51, no. 7, pp. 1–14, Jul. 2019, doi: 10.1007/s11082-019-1924-7.

[23] A. N. Taheri and H. Kaatuzian, "Simulation and design of a submicron ultrafast plasmonic switch based on nonlinear doped silicon MIM waveguide," *J. Comput. Commun.*, vol. 1, no. 7, pp. 23–26, Nov. 2013, doi: 10.4236/jcc.2013.17006.

[24] M. Rahmatiyar, M. Afsahi, and M. Danaie, "Design of a refractive index plasmonic sensor based on a ring resonator coupled to a MIM waveguide containing tapered defects," *Plasmonics*, vol. 15, pp. 2169–2176, Dec. 2020, doi: 10.1007/s11468-020-01238-z.

[25] M. Butt, S. N. Khonina, and N. L. Kazanskiy, "Plasmonics: A necessity in the field of sensing – A review," *Fiber Integr. Opt.*, vol. 40, no. 1, pp. 14–47, Jan. 2021, doi: 10.1080/01468030.2021.1902590.

[26] L. Chen et al., "Numerical analysis of a near-infrared plasmonic refractive index sensor with high figure of merit based on a fillet cavity," *Opt. Exp.*, vol. 24, no. 9, pp. 9975–9983, May 2016, doi: 10.1364/OE.24.009975.

[27] V. Najjari, S. Mirzanejhad, and A. Ghadi, "Plasmonic refractive index sensor and plasmonic bandpass filter including graded 4-step waveguide based on Fano resonances," *Plasmonics*, vol. 17, pp. 1809–1817, Aug. 2022, doi: 10.1007/s11468-022-01667-y.

[28] X.-M. Geng, T.-J. Wang, D.-Q. Yang, L.-Y. He, and C. Wang, "Tunable plasmonic wavelength demultiplexing device using coupled resonator system," *IEEE Photon. J.*, vol. 8, no. 3, Jun. 2016, Art. no. 4801908, doi: 10.1109/JPHOT.2016.2573041.

[29] Z. Chen et al., "Spectral splitting based on electromagnetically induced transparency in plasmonic waveguide resonator system," *Plasmonics*, vol. 10, pp. 721–727, Jun. 2015, doi: 10.1007/s11468-014-9858-1.

[30] Y. D. Wu, "High transmission efficiency wavelength division multiplexer based on metal–insulator–metal plasmonic waveguides," *J. Lightw. Technol.*, vol. 32, no. 24, pp. 4242–4246, Dec. 2014, doi: 10.1109/JLT.2014.2359938.

[31] K. A. Catchpole and A. Polman, "Plasmonic solar cells," *Opt. Exp.*, vol. 16, no. 26, pp. 21793–21800, Dec. 2008, doi: 10.1364/OE.16.021793.

[32] P. Mandal, "Application of plasmonics in solar cell efficiency improvement: A brief review on recent progress," *Plasmonics*, vol. 17, pp. 1247–1267, Jun. 2022, doi: 10.1007/s11468-022-01616-9.

[33] B. Ai, Z. Fan, and Z. J. Wong, "Plasmonic–perovskite solar cells, light emitters, and sensors," *Microsystems Nanoeng.*, vol. 8, no. 1, Jan. 2022, Art. no. 5, doi: 10.1038/s41378-021-00334-2.

[34] S. Liu, Y. Sun, L. Chen, Q. Zhang, X. Li, and J. Shuai, "A review on plasmonic nanostructures for efficiency enhancement of organic solar cells," *Mater. Today Phys.*, vol. 24, May 2022, Art. no. 100680, doi: 10.1016/j.mtphys.2022.100680.

[35] M. S. I. Sumon, M. O. Sharif, A. B. M. R. Anwar, S. S. Mahmud, and R. H. Sagor, "Theoretical investigation of a GaAs based novel air slot nanoplasmonic coupler," in *Proc. IEEE Region 10 Symp.*, 2020, pp. 1123–1127, doi: 10.1109/TENSYMP50017.2020.9230972.

[36] S. A. Dereshgi and A. K. Okyay, "Large area compatible broadband superabsorber surfaces in the VIS-NIR spectrum utilizing metal-insulator-metal stack and plasmonic nanoparticles," *Opt. Exp.*, vol. 24, no. 16, pp. 17644–17653, Aug. 2016, doi: 10.1364/OE.24.017644.

[37] S. Mubeen, J. Lee, W.-R. Lee, N. Singh, G. D. Stucky, and M. Moskovits, "On the plasmonic photovoltaic," *Amer. Chem. Soc. Nano*, vol. 8, no. 6, pp. 6066–6073, Jun. 2014, doi: 10.1021/nn501379r.

[38] M. Heydari and M. Sabaeian, "Plasmonic nanogratings on MIM and SOI thin-film solar cells: Comparison and optimization of optical and electric enhancements," *Appl. Opt.*, vol. 56, no. 7, pp. 1917–1924, Mar. 2017, doi: 10.1364/AO.56.001917.

[39] R. H. Sagor, M. S. I. Sumon, and M. Tazwar, "Design and analysis of a novel air gap–based semi-elliptical nanoplasmonic coupler," *Plasmonics*, vol. 14, pp. 1993–2001, Dec. 2019, doi: 10.1007/s11468-019-00993-y.

[40] G. Veronis and S. Fan, "Theoretical investigation of compact couplers between dielectric slab waveguides and two-dimensional metal-dielectric-metal plasmonic waveguides," *Opt. Exp.*, vol. 15, no. 3, pp. 1211–1221, Feb. 2007, doi: 10.1364/OE.15.001211.

[41] S. H. Badri and M. M. Gilarlue, "Coupling between silicon waveguide and metal-dielectric-metal plasmonic waveguide with lens-funnel structure," *Plasmonics*, vol. 15, pp. 821–827, Jun. 2020, doi: 10.1007/s11468-019-01085-7.

[42] R. A. Wahsheh, "Theoretical investigation of an air-slot mode-size matcher between dielectric and MDM plasmonic waveguides," *Int. J. Opt.*, vol. 2021, pp. 1–8, 2021, doi: 10.1155/2021/1025374.

[43] R. A. Wahsheh and M. A. Abushagur, "Experimental and theoretical investigations of an air-slot coupler between dielectric and plasmonic waveguides," *Opt. Exp.*, vol. 24, no. 8, pp. 8237–8242, Apr. 2016, doi: 10.1364/OE.24.008237.

[44] R. A. Wahsheh, "Mode coupling enhancement from dielectric to plasmonic waveguides," *Opt. Eng.*, vol. 59, no. 10, Oct. 2020, Art. no. 107101, doi: 10.1117/1.OE.59.10.107101.

[45] R. A. Wahsheh, "Efficient and ultra-compact nanoplasmonic Mach-Zehnder interferometer design using air-gap couplers," *Front. in Opt.*, Washington, DC, USA, Nov. 2021, Paper JTu1A.124, doi: 10.1364/FIO.2021.JTu1A.124.

[46] R. A. Wahsheh, "Evaluation of the coupling characteristics of a sandwiched plasmonic waveguide between two dielectric waveguides using air-gap couplers to achieve high-performance optical interconnects," *Opt. Eng.*, vol. 61, no. 10, pp. 107111–107111, Oct. 2022, doi: 10.1117/1.OE.61.10.107111.

[47] R. Charbonneau, N. Lahoud, G. Mattiussi, and P. Berini, "Demonstration of integrated optics elements based on long-ranging surface plasmon polaritons," *Opt. Exp.*, vol. 13, no. 3, pp. 977–984, Feb. 2005, doi: 10.1364/OPEX.13.000977.

[48] R. Charbonneau et al., "Passive integrated optics elements based on long-range surface plasmon polaritons," *J. Lightw. Technol.*, vol. 24, no. 1, pp. 477–494, Jan. 2006, doi: 10.1109/JLT.2005.859856.

[49] C. Manolatou, H. A. Haus, C. Manolatou, and H. A. Haus, "High density integrated optics," *Passive Compon. Dense Opt. Integration*, vol. 17, no. 9, pp. 97–125, Sep. 2002, doi: 10.1109/50.788575.

[50] J. S. Jensen and O. Sigmund, "Topology optimization of photonic crystal structures: A high-bandwidth low-loss T-junction waveguide," *J. Opt. Soc. Amer. B*, vol. 22, no. 6, pp. 1191–1198, Jun. 2005, doi: 10.1364/josab.22.001191.

[51] A. Noual, A. Akjouj, Y. Pennec, J. N. Gillet, and B. Djafari-Rouhani, "Modeling of two-dimensional nanoscale Y-bent plasmonic waveguides with cavities for demultiplexing of the telecommunication wavelengths," *New J. Phys.*, vol. 11, no. 10, Oct. 2009, Art. no. 103020, doi: 10.1088/1367-2630/11/10/103020.

[52] J. Tian, R. Yang, L. Song, and W. Xue, "Optical properties of a Y-splitter based on hybrid multilayer plasmonic waveguide," *IEEE J. Quantum Electron.*, vol. 50, no. 11, pp. 898–903, Nov. 2014, doi: 10.1109/JQE.2014.2359232.

[53] R. Rahad, A. K. M. Rakib, M. A. Haque, S. S. Sharar, and R. H. Sagor, "Plasmonic refractive index sensing in the early diagnosis of diabetes, anemia, and cancer: An exploration of biological biomarkers," *Results Phys.*, vol. 49, Jun. 2023, Art. no. 106478, doi: 10.1016/j.rinp.2023.106478.